Received 3 November 2022; accepted 27 November 2022. Date of publication 2 December 2022; date of current version 13 December 2022.

*Digital Object Identifier 10.1109/OJAP.2022.3226275*

# Optimum Antenna Characteristics for Maximally Harvesting Ambient RF Energy

**CONSTANT M. A. NIAMIEN (Member, IEEE)**

Research Institute of Embedded Electronic Systems, Normandie Univ, UNIROUEN, ESIGELEC, IRSEEM, 76000 Rouen, France

CORRESPONDING AUTHOR: C. M. A. NIAMIEN (e-mail: constant.niamien@esigelec.fr)

This work was supported in part by Project SURFAS, an Interreg France (Channel) England Cross-Border Cooperation Project, which is cofinanced by ERDF.

**ABSTRACT** This paper investigates the best antenna characteristics to harvest ambient RF waves maximally. The proposed approach analyzes and compares key design aspects, including multi-polarization, multi-port, multi-band, omnidirectional, quasi-isotropic, and non-quasi-isotropic pattern options, over the same antenna size defined by the enclosing sphere radius. First, the ideal isotropic and the Dirac-directive antennas are theoretically analyzed and compared within a general Gaussian channel to derive the most suitable design options. Then, several test antennas, covering the design options, are designed, fabricated, characterized, and compared within a full-wave antenna simulator under spherical incidences and polarizations. Further experiments in real ambient environments complete the tests. Two optimum antenna solutions emerge from the results: the quasi-isotropic antenna and the collocated LP-port diversity system with a power combiner. The crucial feature is optimizing antenna solutions for lower frequency bands with significant power densities that compensate for the available power $\lambda^2$-factor.

**INDEX TERMS** Dipole antennas, directive antennas, isotropic antennas, energy harvesting, receiving antennas.

## I. INTRODUCTION

A STANDARD ambient radio-frequency (RF) harvesting system, as presented in Fig. 1, includes an antenna, a matching circuit, a rectifying circuit, and a power management circuit (PMC). The antenna captures the surrounding electromagnetic (EM) waves, driven to the antenna port, and transferred to the rectifying circuit via an impedance matching circuit, maximizing power transfer. It is worth mentioning that the antenna may cover the matching circuit functionality for simplification, loss reduction, and increased performance [1], [2], [3], [4]. The PMC boosts and compensates for the continuously varying level of the rectified power (direct current, DC) to feed the terminal low-power device, such as a sensor, a detector, etc. Therefore, each block plays a key role in the system's operation and performance. However, incident waves are the most critical factors shaping the system performance within the ambient environment. Indeed,

i) incident waves behave randomly over time and space, including polarization, amplitude, and phase distributions [5, pp. 13–16], [6], [7]. This raises the question of the appropriate antenna that can optimally harvest such changing EM waves. Within a deterministic propagation medium, the use of a PMC is questionable unless it serves as a power booster.
ii) Incident waves often carry low RF power densities spreading over a large frequency spectrum, including frequency modulation (FM) up to wireless fidelity (Wi-Fi) bands [8], [9]. This imposes the receiving antenna and the other RF blocks to cope with wideband or multi-band options.
iii) The rectifying circuit's efficiency increases with the input RF power level [10], which means that low harvested RF power produces poor DC power, unable to switch on the PMC to feed the device.

Therefore, one of the most significant challenges in ambient RF energy harvesting is optimizing the entry block, typically the receiving antenna, to maximize the harvested RF power and increase the system's capability to feed the terminal device.

Several approaches emphasize design aspects, such as polarization, number of ports, frequency bands or tones,

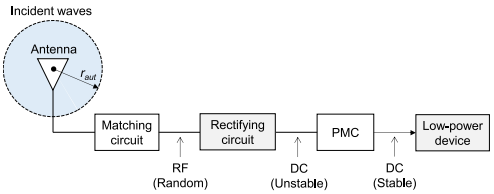


**FIGURE 1.** Architecture of a standard ambient RF energy harvesting system. The antenna may include the matching circuit for simplification, loss reduction, and better performance, as designated as *antenna matching* [1], [2], [3], [4].

and spatial arrangement [11], [12], [13], [14], [15], [16], [17], [18], [19], [20], [21]. Indeed, recently, a two-port dual linearly-polarized (LP) bowtie-shaped meander dipole harvested up to 1.6 times more DC power than the equivalent LP dipole [11]. This work considered a fixed transmitting horn antenna and rotated the receiving antenna to include various polarization mismatch angles. Another example considered a four-port patch antenna with two integrated T-shaped slots. This antenna had two LP ports to receive and transmit simultaneously (full-duplex) while harvesting wireless power on two other LP ports [12]. Besides, other works focused on circular polarization (CP), trying to receive right-hand (RH) and left-hand (LH) CP signals on two ports separately over a single design. These studies used a patch antenna with two-coupled crossed slots [13] or a star-like slot coupled to a dielectric resonator antenna [14]. However, even though these works showed dual-polarization benefits [11], [12], [13], [14], they omitted to compare with a reference single-polarized antenna within the "real" operating environment carrying multiple incidences simultaneously.

On the other hand, some works focused on multi-band, wideband, and multi-tone aspects [15], [16]. Indeed, the work in [15] employed a wideband single-port dual LP bowtie dipole with a ground reflector, harvesting almost four times higher voltage with four simultaneous tones than a single tone. Another example in [16], based on a single-port dual CP log-periodic crossed bowtie dipole, covered up to six bands. This antenna exhibited 26 $\mu$W more DC power than [15], attributed to the additional covered bands and possible CP benefits over LP.

Finally, some approaches use electrically small antennas in array sets to increase the effective area and boost the harvested power through the number of harvesters over the same array size [20], [21]. Besides, other approaches combined wideband or multi-band, dual-polarization, multi-port, and array sets to significantly increase the harvested power. Indeed, the work in [17] considered a two-dimensional (2D) dual-band array of 16 orthogonal LP inverted-F antennas (IFA) to harvest 13 dB (20 times) more DC power than a single-band IFA. Other similar approaches scale the array size to 64 elements based on a CP equiangular spiral antenna [18], [19]. In addition, different approaches consider several multi-beam arrays to realize a quasi-isotropic coverage sequentially with high directivity [1], [22], [23], [24]. This technique shows up to 3.4 or 4.6 times more DC power than an equivalent 3-dipole linear array fitting in the same size [22].

Despite the variety of the design options addressed, typically dual-polarization, wideband, multi-band, multi-port, multi-beam, small antenna, and array set, most works do not include the isotropic pattern option on a single antenna element. This is essential for harvesting incident waves from any direction. In addition, the testing conditions often cover a single incidence with two principal polarizations, neglecting the complete spherical coverage of the antenna pattern and its complex interaction with the incident wavefield. Table 1 summarizes the most relevant works' features and limitations.

This paper fulfills these gaps by deriving the best antenna characteristics to harvest ambient waves maximally. The proposed approach analyzes and compares key design aspects, such as multi-polarization, multi-port, multi-band, omnidirectional, quasi-isotropic, and non-quasi-isotropic pattern options on the same antenna size. First, the ideal isotropic and the Dirac-directive antennas are theoretically analyzed and compared within a general Gaussian propagation channel to derive the most suitable design option. Next, various test antennas, covering the design options, are compared within a full-wave antenna simulator under spherical incidences and polarizations. Finally, the antennas are fabricated, characterized, and tested within the ambient environment in various locations.

This paper is organized as follows. First, Section II theoretically analyzes and compares the ideal isotropic antenna with the Dirac-directive one to derive the most suitable for receiving ambient waves. Then, Section III presents a set of test antennas covering various design aspects. Finally, Sections IV and V validate the optimum antenna characteristics for maximally receiving ambient waves through numerical tests and experiments in actual conditions.

## II. THEORETICAL BASIS

### A. PRELIMINARY DEFINITIONS

Let us consider the general receiving antenna within the ambient environment, supporting non-line-of-sight (NLOS) propagation waves. This is a Rayleigh-fading propagation environment [5, pp. 13–16], [6], demonstrated in indoor and outdoor propagation media over most mobile frequency bands [6], [9]. Therefore, this propagation medium is assumed throughout the paper, referred to as ambient waves in the following sections.

The time-averaged power received by the antenna is a key performance indicator, expressed with the average available power $P_{ref}$ (reference power) as [5, p. 138]:

$$P_{rec} = \left\{ \frac{X}{X+1} \int_{\Omega} p_\theta G_\theta d\Omega + \frac{1}{X+1} \int_{\Omega} p_\phi G_\phi d\Omega \right\} P_{ref} \quad (1)$$

where $\Omega$ is the solid angle defined at the observation point, $X$ represents the cross-polarization ratio, that is, the ratio of the reference $\theta$-polarized power to the $\phi$-polarized one,

**TABLE 1.** Summary of the most relevant works' features and limitations.

| | | Design options | | | | | Testing conditions | | | |
|---|---|---|---|---|---|---|---|---|---|---|
| Ref. | Antenna geometry | Polarization (type) | Port | Frequency band/tone (GHz) | Spatial arrangement | Isotropic option | Harvesting system, Power combination | Controlled environment | | Ambient |
| | | | | | | | | Incidence | Polarization | |
| [11] | Bowtie-shaped meandered dipoles | Single, Dual (LP) | 1, 2 | Single (2.45) | Collocation | No | Rectenna, DC | Single (horn) | Dual (LP) | No |
| [12] | Patch antenna with two integrated T-shaped slots | Dual (LP) | 4 | Single (2.45) | Symmetric array | No | Antenna, No | No | --- | No |
| [13] | Two crossed slots coupled to a patch antenna | Dual (CP) | 2 | Single (2.45) | Stacking | No | Antenna, No | No | --- | No |
| [14] | A star-like slot coupled to a dielectric resonator cube | Dual (CP) | 2 | Broad (1.83-2.85) | Stacking | No | Antenna, No | No | --- | No |
| [15] | Bowtie dipole with a reflector plane | Dual (LP) | 1 | Four (0.9, 1.8, 2.1, 2.4) | Collocation + Stacking | No | Rectenna, DC | Single (dipole) | Single (LP) | No |
| [16] | Log-periodic crossed bowtie dipole | Dual (CP) | 1 | Six (0.55, 0.75, 0.9, 1.85, 2.15, 2.45) | Collocation + Stacking | No | Rectenna, DC | No | No | Yes (indoor, outdoor) |
| [17] | Inverted-F antenna | Dual (LP) | 16 | Dual (0.94, 1.84) | 2D-array of orthogonal antennas | No | Rectenna, DC | Single | Dual (LP) | Yes (outdoor) |
| [19] | Equiangular spiral antenna | Dual (CP) | 64 | Broad (2-8) | 2D-array | No | Rectenna, DC | Single | Single (LP) | No |
| [20] | T-shaped slot (ESA*) | Single (LP) | 6 | Single (0.9) | 2D-array of ESA | No | Rectenna, DC | Single | Single (CP) | Yes** (indoor) |
| [22] | Patch antenna | LP | 4 | Single (2.4) | 1D-array + cylindrical bending | Yes*** | Rectenna, DC | Single | Single | Yes** (indoor) |
| This work | Collocated straight crossed dipoles | Single, Dual, Triple (LP, CP) | 1, 2, 3 | Dual (0.94, 1.84) | Collocation | Yes | Antenna, RF | Spherical (3D simulator) | Dual (Spherical) | Yes (indoor) |

LP: Linearly polarized, CP: Circularly polarized. (*) ESA: electrically small antenna, (**) controlled transmitter, (***) This antenna considers a cylindrically bent linear array associated with a Butler matrix to form a multi-beam multi-port array offering a sequential quasi-isotropic coverage in azimuth.

$X = P_{ref\theta}/P_{ref\phi}$, while $P_{ref} = P_{ref\theta} + P_{ref\phi}$. The angular functions $p_\theta$ and $p_\phi$ represent the incident power spatial distributions in vertical and horizontal polarizations, respectively. The corresponding normalization expressions are:

$$\int_\Omega p_\theta d\Omega = \int_\Omega p_\phi d\Omega = 1 \tag{2}$$

In (1), $G_\theta$ and $G_\phi$ represent the antenna realized gain in vertical and horizontal polarizations, respectively. The total realized gain $G = G_\theta + G_\phi = \eta_t D$, is linked to the effective area $A_{eff}$ by [16]:

$$A_{eff} = \frac{\lambda^2 G}{4\pi} = \eta_t \frac{\lambda^2 D}{4\pi} \tag{3}$$

where $D$ is the antenna directivity, $\eta_t = \tau\eta_r$, the total efficiency, $\eta_r$, the radiation efficiency, and $\tau$ is a transmission coefficient between the antenna port and the remaining circuit, including a transmission line and a load. Please refer to [25] for the complete expression of $\tau$. However, for simplicity, $\tau = 1$ is assumed throughout the paper. This indicates a "perfect" impedance matching between the antenna port and the remaining circuit (no mismatch loss).

### B. OPTIMUM RECEIVING ANTENNA UNDER AMBIENT WAVES

This section analyzes the average received power, $P_{rec}$, of several special antennas within ambient waves. All antennas are matched and 100%-efficient, that is, $\eta_t = 1$.

#### 1) IDEAL ISOTROPIC ANTENNA

In the particular case of an ideal $\theta$-polarized isotropic antenna, with $G_\theta = D_\theta = 1$ and $G_\phi = D_\phi = 0$, (1) gives:

$$P_{rec-iso\theta} = \frac{XP_{ref}}{X+1}\eta_t = P_{ref\theta} \tag{4}$$

Similarly, the ideal $\phi$-polarized isotropic antenna receives:

$$P_{rec-iso\phi} = \eta_t P_{ref\phi} = P_{ref\phi} \tag{5}$$

Therefore, the system of two ideal isotropic antennas, perfectly matched and 100%-efficient, receives the entire available power in both $\theta$- and $\phi$-polarizations on a time average. Moreover, this result stands regardless of the incident waves' spatial distributions $(p_\theta, p_\phi)$.

#### 2) IDEAL DIRAC-DIRECTIVE ANTENNA

Let us consider an ideal directive antenna, which is $\theta$-polarized and whose gain is maximum in a particular direction $\Omega = \Omega_{0\theta}$, that is, $G = G_{0\theta}\delta(\Omega - \Omega_{0\theta})$, where $\delta$ is the Dirac distribution. According to (1), this Dirac-directive antenna receives

$$P_{rec-Dirac\theta} = P_{ref\theta} p_{0\theta} G_{0\theta} \tag{6}$$

where $p_{0\theta} = p_\theta(\Omega_{0\theta})$ is the $\theta$-polarized channel value in the maximum gain's direction. However, invoking the normalization condition (2) in $\int G d\Omega = 4\pi\eta_t$, leads to:

$$G_{0\theta} = 4\pi\eta_t = 4\pi \tag{7}$$

where $\int \delta(\Omega - \Omega_{0\theta})\mathrm{d}\Omega = 1$.

Therefore, the condition for the Dirac-directive antenna to receive equal or more power than the ideal isotropic antenna in $\theta$-polarization is $P_{rec-Dirac\theta} \geq P_{ref\theta}$, that is,

$$p_{0\theta} \geq \frac{1}{4\pi} \tag{8}$$

Let us now analyze (8) by plotting $p_\theta$ for a general propagation channel which is Gaussian-type with elevation angle $\theta$ and isotropic with azimuth $\phi$. That is:

$$p_\theta(\theta, \phi) = A_\theta e^{\frac{-(\theta-\theta_{c\theta})^2}{2\sigma_\theta^2}} \tag{9}$$

where $0 \leq \theta \leq \pi$, and $0 \leq \phi \leq 2\pi$.

Invoking (2) provides the value of $A_\theta$ as:

$$A_\theta = \frac{1}{2\pi \int_0^\pi \sin\theta e^{\frac{-(\theta-\theta_{c\theta})^2}{2\sigma_\theta^2}} d\theta} \tag{10}$$

where $\theta_{c\theta}$ is the elevation angle of the channel's maximum value, while the standard deviation of the channel is $\sigma_\theta$.

From (9), it is straightforward to see that $A_\theta$ is the channel's maximum value. It depends on $\sigma_\theta$, but not on $\theta_{c\theta}$. Therefore, Fig. 2a plots $A_\theta$ as a function of $\sigma_\theta$ for a given value of $\theta_{c\theta} = 90° - \mathrm{m}_{c\theta} = 70°$, where $m_{c\theta} = 20°$ is a standard value for a $\theta$-polarized Gaussian channel in indoor and outdoor environments on the Global System for Mobile communication band (GSM 900: 880-960 MHz) [6], [9], [26]. In addition, Fig. 2b plots $p_\theta$ as a function of $\theta$ for several values of $\sigma_\theta$ ranging from 20 to 200 step 20, with $\theta_{c\theta} = 70°$.

Fig. 2a indicates that the lower bound of $A_\theta$ is $1/4\pi$, the isotropic channel distribution value. Therefore,

$$A_\theta \geq \frac{1}{4\pi} \forall \sigma_\theta \tag{11}$$

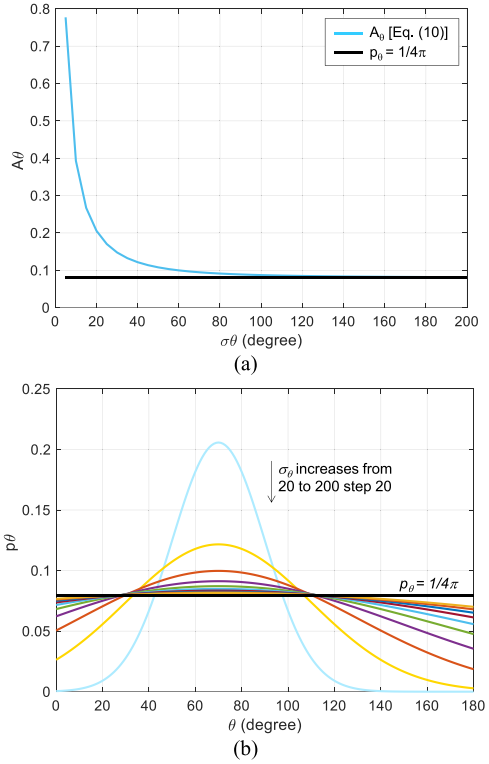


**FIGURE 2.** Gaussian channel characteristics, (a): channel's maximum value $A_\theta$ as a function of $\sigma_\theta$, (b): channel distribution $p_\theta$ with elevation angle $\theta$. Both plots assume $\theta_{c\theta} = 90° - \mathrm{m}_{c\theta} = 70°$, where $m_{c\theta} = 20°$ is a standard value for a $\theta$-polarized Gaussian channel in indoor and outdoor environments over GSM 900-band.

Inequality (11) means that (8) is always true whenever the Dirac-directive antenna focuses on the channel's maximum value direction $\Omega_c(\theta_{c\theta}, \phi_{c\theta})$. In this case, it systematically receives more power than the isotropic antenna. However, this result collapses when there is misalignment. Indeed, Fig. 2b indicates that not so far from the channel's maximum value direction, the Gaussian channel values drop rapidly and get below the isotropic channel value of $p_\theta = 1/4\pi$. For instance, this occurs for $\theta \leq 42°$ and $\theta \geq 97°$ for the case of $\sigma_\theta = 20°$. This range in which the isotropic antenna outperforms the Dirac-directive antenna increases as $\sigma_\theta$ decreases, corresponding to an increasingly directive channel. Beyond that, it is worth mentioning that the particular case of the $\phi$-polarized Dirac-directive antenna leads to the same results and analyses.

### C. SUMMARY

According to previous Sections II-B1 and II-B2, the following conclusions are made:

i) The ideal isotropic antenna receives the entire time-averaged available power in $\theta$- and $\phi$-polarizations, regardless of the channel's spatial distributions.
ii) The ideal directive antenna receives more power than the ideal isotropic antenna as long as the former precisely focuses on the channel's maximum value direction. Besides, like any arbitrary antenna, both antennas capture the same power within an isotropic channel.

iii) Any misalignment between the ideal directive antenna and the channel's maximum value direction leads to power loss, leading the isotropic antenna to outperform the ideal directive antenna within a dedicated elevation angle range. This range increases as the channel tends to be more directive.

iv) Realizing the above antenna-channel alignment in ii) is tricky within a Rayleigh-fading environment (NLOS) since this suggests a precise preconception of the channel's space-time behavior for any frequency band of interest. Indeed, this means knowing the RF source characteristics (number, position, radiation pattern, transmitting power, etc.) and mainly the propagation loss factors, models, etc. Unfortunately, anticipating these parameters with accuracy is almost impossible for any location, considering standard wireless applications [27, ch. 4–5].

v) Based on i), iii), and iv), the ideal isotropic antenna is the most suitable receiving antenna within the ambient environment since it is channel-insensitive to capture the available power. However, the directive antenna remains the best option within a predefined or deterministic propagation environment.

vi) The above conclusions also stand for any directive or quasi-isotropic antennas which underperform the ideal antennas with the same behavior. For this reason, the following sections focus on quasi-isotropic antennas.

vii) Finally, even though the proposed formulation stands for Gaussian and isotropic channels within a Rayleigh-type fading environment, a similar approach may be followed to deal with other channel distributions. Beyond that, the above conclusions also cover a Rice-type fading environment, including a deterministic channel component and a random one [7]. The dominant channel component will decide the most suitable antenna based on v).

### D. TIME-AVERAGED AVAILABLE POWER

This section formulates the time-averaged available power ($P_{ref}$) with the space-time-averaged power density $W_{inc}$. According to previous Section II-B1, the $\theta$-polarized (resp. $\phi$-polarized) isotropic antenna captures $P_{ref\theta}$ (resp. $P_{ref\phi}$). Therefore, invoking (3) allows expressing the elementary time-averaged power per unit solid angle $d\Omega$ with the time-averaged power density $w_{inc\theta}$ in direction $\Omega$ as:

$$\frac{dP_{ref\theta}}{d\Omega} = A_{eff\theta} w_{inc\theta} = \frac{\lambda^2}{4\pi} w_{inc\theta} \tag{12}$$

where $w_{inc\theta}$ is linked to $p_\theta$ by:

$$p_\theta(\Omega) = \frac{w_{inc\theta}(\Omega)}{\int_\Omega w_{inc\theta}(\Omega) d\Omega} \tag{13}$$

Now, let us consider the following approximation:

$$\int_\Omega w_{inc\theta}(\Omega) d\Omega \approx \int_\Omega W_{inc\theta} d\Omega = 4\pi W_{inc\theta} \tag{14}$$

where $W_{inc\theta}$ is the spatial average of $w_{inc\theta}$.

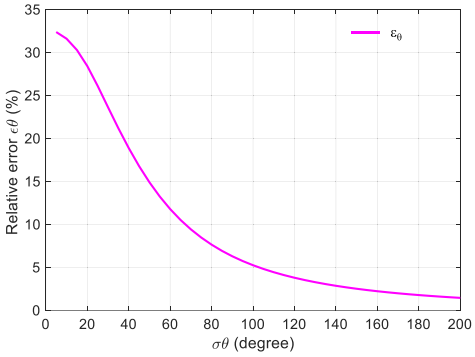


**FIGURE 3.** Relative error $\varepsilon_\theta$ obtained from (15) and plotted for the Gaussian channel as a function of $\sigma_\theta$.

It is straightforward to derive the relative error of (14) as:

$$\varepsilon_\theta = \frac{\int_\Omega w_{inc\theta}(\Omega) d\Omega - \int_\Omega W_{inc\theta}(\Omega) d\Omega}{\int_\Omega w_{inc\theta}(\Omega) d\Omega} = 1 - 4\pi \overline{p}_\theta \tag{15}$$

where $\overline{p}_\theta$ represents the spatial average of $p_\theta$.

Fig. 3 plots $\varepsilon_\theta$ for the $\theta$-polarized Gaussian channel as a function of $\sigma_\theta$.

Fig. 3 indicates that the error rapidly decreases with $\sigma_\theta$. Therefore, the error reaches 33% for highly directive channels (low $\sigma_\theta$) and vanishes toward isotropic channels (high $\sigma_\theta$). In practice, the $\theta$-polarized channel in indoor and outdoor environments over most wireless communications, including GSM 900 up to Wi-Fi 2.45 GHz, can be assumed as isotropic in a first-order approximation. In this viewpoint, the error made is negligible. However, in a more precise approach, the channel is often assumed Gaussian with a standard deviation $\sigma_\theta$ between 20 and 100° [6], [9], [26]. This case sets $\varepsilon_\theta$ between 5 and 28%, which is acceptable.

Integrating (12) over the 3D space while invoking (13) – (14) leads to:

$$P_{ref\theta} = \int_\Omega dP_{ref\theta} \approx \lambda^2 W_{inc\theta} \tag{16}$$

Since the exact derivation applies to $\phi$-polarized waves, (16) still stands for $P_{ref\phi}$ by just replacing $\theta$ with $\phi$. Therefore, the total available power reads:

$$P_{ref} \approx \lambda^2 \left( W_{inc\theta} + W_{inc\phi} \right) \tag{17}$$

where the cross-polarization ratio also reads as:

$$X = \frac{P_{ref\theta}}{P_{ref\phi}} \approx \frac{W_{inc\theta}}{W_{inc\phi}} \tag{18}$$

From (16) – (17), one can make the following analyses:

i) The time-averaged available power in each polarization increases with $\lambda^2$, and the space-time-averaged power density $W_{inc}$. Fig. 4 illustrates this result by plotting (16) up to 6 GHz for several values of $W_{inc}$ ranging from 0.01 to 10 nW/cm$^2$.

ii) Given two frequency bands around $f_1$ and $f_2$ ($f_2 > f_1$) with the same power density $W_{inc}$, $P_{ref}$ ($f_1$) is $(f_2/f_1)^2$ times higher than $P_{ref}(f_2)$. For instance, for

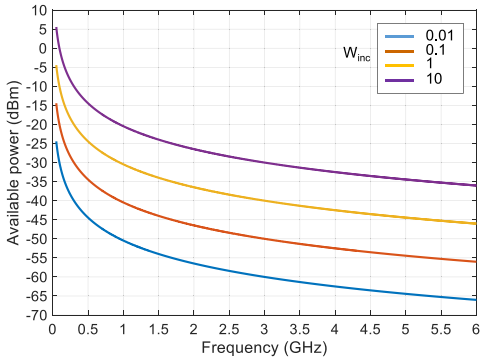


**FIGURE 4.** Time-averaged available power as a function of frequency for various space-time-averaged power densities $W_{inc}$ in nW/cm$^2$. This plot concerns single-polarized incident waves, either $\theta$- or $\phi$-polarizations.

$W_{inc} = 1\ nW/cm^2$, $P_{ref}(940\ MHz) \approx -29.92$ dBm while $P_{ref}(1840\ MHz) \approx -35.75$ dBm, leading to a power decrease factor of almost 6 dB.

iii) Considering a higher-frequency receiving antenna suggests compensating for the $\lambda^2$-power factor, like [17] increasing the number of antennas accordingly.

iv) Therefore, the optimum single-band or multi-band receiving antenna within the ambient environment is the one targetting lower frequencies or those for which the power density compensates for the $\lambda^2$-factor.

### E. TIME-AVERAGED HARVESTED DC POWER

Even though the focus is on the antenna part, this section analyzes the time-averaged harvested DC power.

The harvested DC power entering the PMC is linked to the conversion efficiency ($\eta_{RF-DC}$) and the RF power received by the antenna ($P_{RF}$) by:

$$P_{DC} = \eta_{RF-DC} P_{RF} \tag{19}$$

According to [28], under the diode's breakdown point, $\eta_{RF-DC}$ is linearly dependent on $P_{RF}$, meaning that $P_{DC}$ is proportional to the square of $P_{RF}$. Therefore, maximizing $P_{RF}$ maximizes $P_{DC}$ systematically. Moreover, this behavior extends to the time-averaged powers, $P_{rec}$ and $P_{DCavg}$. Thus, based on (1) and (17) and assuming the diode's junction resistance ($R_j$) is much greater than the series resistance ($R_s$), $R_j >> R_s$, the time-averaged DC power under matching conditions is formulated as:

$$P_{DCavg} \approx \underbrace{\left(\frac{\lambda^4}{\lambda^2 + \lambda_j^2}\right)}_{F} \cdot \underbrace{\left(\frac{\Re_I \sqrt{R_j}}{2}\right)^2}_{D} \cdot MEG^2 \cdot \left(W_{inc\theta} + W_{inc\phi}\right)^2 \tag{20}$$

where $\lambda_j = 2\pi c C_j \sqrt{(R_s R_j)}$ is a characteristic wavelength linked to the diode's cutoff frequency, $f_j = c/\lambda_j$; $c$ is light's speed in free space, while $C_j$ and $\Re_I$ denote the diode's junction capacitance and current responsivity, respectively.

**TABLE 2.** Specifications of the test antennas.

| | Design options | | | |
|---|---|---|---|---|
| **Test antennas** | **Bands** | **Pol.** | **Ports** | **Isotropic option** |
| Dipoles ($x$-axis, $y$-axis, $z$-axis) | Single | LP | 1 | No |
| Optimally-fed crossed dipole (Turnstile) | Single | CP* | 1 | Yes |
| In-phase-fed crossed dipole | Single | Dual LP | 1 | No |
| 2-port crossed dipole | Single | Dual LP | 2 | No |
| Optimally-fed tripole | Single | CP* | 1 | Yes |
| In-phase-fed tripole | Single | Triple LP | 1 | No |
| 3-port tripole | Single | Triple LP | 3 | No |
| Dual-band quasi-isotropic dipole | Dual | CP* | 1 | Yes |

Single band = GSM 900-band. Dual-band = GSM 900 + DCS 1800. Pol. = polarization. (*) CP along the z-axis.

MEG is the receiving antenna's mean effective gain [6], [7], defined in (1) in the curly brackets.

In (20), factor $F$ represents the impact of the operating frequency or wavelength, while $D$ includes the diode performance impact. Besides, MEG considers the interaction between the receiving antenna and the incident waves. Beyond that, (20) indicates that the most decisive factor for boosting $P_{DCavg}$ is the operating frequency or wavelength, acting as a power-four term (or higher). In contrast, the other factors ($D$, $MEG$, $W_{inc}$) have a power-two impact. Indeed, $F$ behaves as $\lambda^4$ at low frequencies ($\lambda >> \lambda_j$) but follows $\lambda^8$ for higher frequencies ($\lambda << \lambda_j$).

Overall, maximizing $P_{DCavg}$ means optimizing the antenna with the propagation medium to get the highest $MEG$ and choosing the most suitable diode with the highest $D$. Prior to that, it is crucial anticipating the operating frequency and the available power densities to maximize $F^*(W_{inc\theta} + W_{inc\phi})^2$.

The following sections focus on the antenna part only as the DC power follows the received RF power's behavior. The analysis will include full-wave simulations and real ambient measurements based on several test antennas.

## III. TEST ANTENNAS

This section presents several test antenna geometries, design steps, and characteristics. This includes reflection coefficient, efficiency, directivity, and realized gain. In addition, results include simulations and measurements. The multi-band option focuses on GSM 900, around 940 MHz, and DCS 1800, about 1840 MHz, corresponding to the center frequencies of the related band downlinks. Table 2 details the test antennas' design options.

The dipoles cover single LP antennas with omnidirectional radiation patterns. While the in-phase-fed dipoles (crossed dipole, tripole) cover non-quasi-isotropic antennas with multiple LP and nulls in both $\theta$- and $\phi$-polarizations. The optimally-fed dipoles, typically the turnstile (2D) and the optimum tripole (3D), are quasi-isotropic antennas with

**TABLE 3.** Dimensions of the fabricated dipole.

| Dipole | Feed |
|---|---|
| $L_D = 127$, $W = 1$ | $L_f = 9.5$, $W_f = 1.55$, $L_g = 11.5$, $W_g = 8$, $d_{via} = 0.6$ |

Dimensions are millimeters (mm).

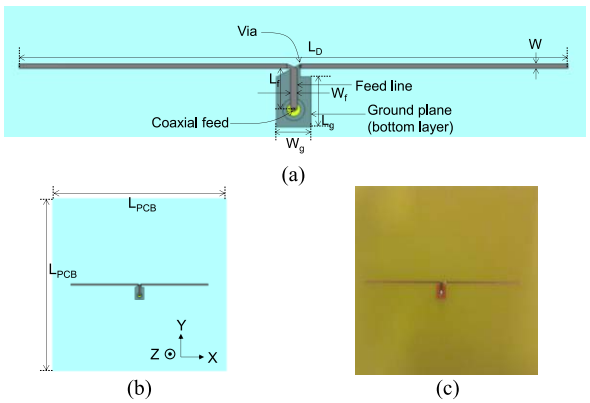


**FIGURE 5.** Dipole antenna, (a): schematic view, (b): overview, (c): photograph of the fabricated dipole prototype.

isotropic patterns in $\phi$-polarization. In $\theta$-polarization, the former has the entire horizontal plane as the null domain, while the latter has "just" a null pair. They radiate CP along the $z$-axis and primarily elliptical polarization everywhere, based on [29].

For comparison needs, all the antennas have the exact occupied area or volume, fitting in the same sphere radius of $r_{aut} \approx L_{PCB}/2$, where $L_{PCB} = 161.4$ *mm* is the size of the square printed circuit board (PCB). Furthermore, the printing substrate is FR4, with claimed permittivity of $\varepsilon_r = 4.2$, and loss tangent of $tan\delta = 0.014$, specified at 2 GHz [30].

Straight dipole-based antenna geometries are used for their design simplicity, allowing antenna collocation with minimum impedance and pattern distortions. Another benefit is their potential to cover several design options, such as quasi-isotropic, non-quasi-isotropic, and omnidirectional patterns, by "just" controlling the feed and the number of elements. Besides, even though more compact antennas may fit the specified size, like in [20], [21], this small antenna design option is not addressed in this study. Therefore, fixed geometries (here, half-wavelength) are suitable to cover the envisioned design options.

### A. DIPOLES

#### 1) THE X-AXIS DIPOLE

This is a standard half-wavelength dipole aligned along the $x$-axis of a Cartesian coordinate system. The dipole length is $L_D$, width, $W$, and operates around 940 MHz.

A microstrip line feeds the dipole through the top conductor, directly connected to one dipole's arm, while the other arm connects to the ground plane through a via.

Fig. 5a gives the schematic view of the dipole, while Fig. 5b presents the overview. In addition, Fig. 5c shows the fabricated prototype's photograph, while Table 3 provides the dimensions of the fabricated prototype.

#### 2) THE Y-AXIS AND Z-AXIS DIPOLES

Rotating the $x$-axis dipole by 90° around the $z$-axis leads to the $y$-axis dipole. Meanwhile, the same rotation around the $y$-axis gives the $z$-axis dipole. Therefore, these rotations do not affect the "intrinsic" performance data, such as the reflection coefficient ($S_{11}$), efficiency, maximum directivity, and gain. However, rotations change the null domains. Indeed, the $y$-axis dipole's radiation patterns consist in rotating those of the $x$-axis dipole by 90° along the $z$-axis. However, the special case of the $z$-axis dipole shows a null in the entire $\phi$-polarization. Please refer to [29] and [37, pp. 182–184] for more details on these dipoles' null domains.

#### 3) THE 3-PORT TRIPOLE

This antenna is a collocated version of the previous three dipoles aligned along the $x$-, $y$-, and $z$-axes. A simplified version of this antenna considered in simulations includes 3-lumped ports for simplification. Simulations, not detailed for brevity, indicate low coupling levels between the dipoles, lower than – 40 dB. Therefore, each dipole in the lattice behaves almost the same as it operates lonely. Full-wave simulations confirm this behavior in the radiation patterns. Consequently, there is no motivation to fabricate this complex design. Instead, rotating the single dipole (Fig. 5c) over three orthogonal positions will sequentially provide this 3-port tripole's experimental results. However, simulations consider the three individual dipoles and the 3-port tripole separately for comparison and validation purposes.

#### 4) THE 2-PORT CROSSED DIPOLE

This antenna is a 2-port version of the previous tripole without the $z$-axis dipole (port #3). Therefore, the previous results of the $x$- and $y$-axis dipoles also represent the 2-port crossed dipole.

### B. SINGLE-PORT SINGLE-BAND TEST ANTENNAS

#### 1) THE OPTIMALLY-FED CROSSED DIPOLE AND TRIPOLE

Figs. 6a – 6d shows the general design's views with the tripole. It is worth mentioning that the tripole includes three printed circuit boards (PCBs), while the crossed dipole design holds on the horizontal PCB only in the $xy$-plane. The two vertical PCBs above and beneath the horizontal PCB include the $z$-axis dipole's arms. The horizontal PCB holds the $x$- and $y$-axis dipoles and includes the feed line, consisting of a primary suspended line ($L_S$, $W_S$), a microstrip impedance transformer ($L_T$, $W_T$), a matching capacitor ($C_M$), and a 50Ω-microstrip line ($L_M$, $W_M$) connected to an SMA connector.

Fig. 7 presents the design steps, summarized as follows:

**Step #1**. Set the initial design parameters according to the following relationships:

$$L \approx \lambda_g/2 \tag{21a}$$

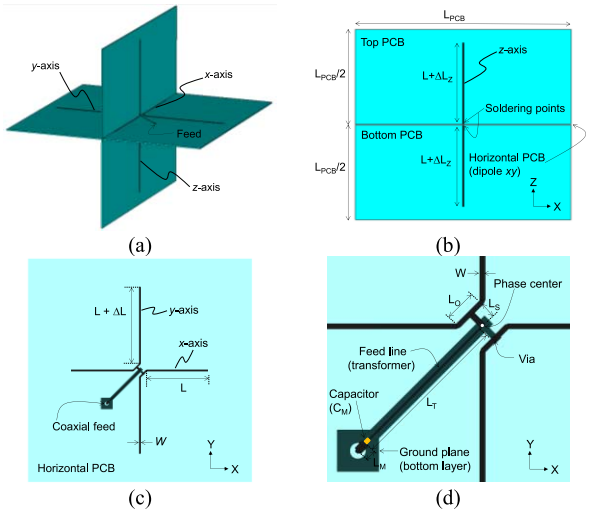


**FIGURE 6.** The single-port tripole, (a): perspective view, (b): sideview in the *zx*-plane, (c): general view of the horizontal PCB, (d): zoom in the horizontal PCB.

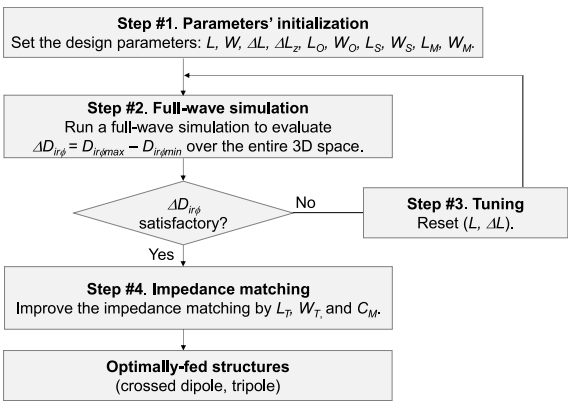


**FIGURE 7.** Design steps of the optimally-fed crossed dipole and tripole.

$$\Delta L \approx L/3 \tag{21b}$$

$$\Delta L_z \approx L_S + L_O/2 + \sqrt{L_S^2 + L_O^2/4} \tag{21c}$$

where $\lambda_g$ is the guided wavelength. The extra length $\Delta L$ on the $y$-axis dipole implements the 90°-phase shift condition [32], while the extra length $\Delta L_z$ on the $z$-axis dipole compensates for the $x$-axis and $y$-axis dipoles' offsets due to lines $L_O$ and $L_S$, introduced to free some space for the feed. Choosing $L_O$ and $L_S$ as low as possible helps minimize the dipoles' offsets from the phase center. Thin or moderately wide dipole arms ($W$) may be used. Besides, the offset line widths may be identical, as $W_O \approx W_S \approx W$.

**Step #2**. Run a full-wave simulation to evaluate the gain or directivity variation, $\Delta D_{ir\phi}(dB) = D_{ir\phi max} - D_{ir\phi min}$, performed over the entire 3D space on the $\phi$-component since only this component can shape an isotropic behavior [29]. If $\Delta D_{ir\phi}(dB)$ is below the target value, often set at 6 dB or lower, this pattern design process stops.

**Step #3**. Whenever $\Delta D_{ir\phi}(dB)$ is not good, the pattern optimization process continues by resetting $L$ and $\Delta L$ and checking $\Delta D_{ir\phi}(dB)$ until getting satisfactory results.

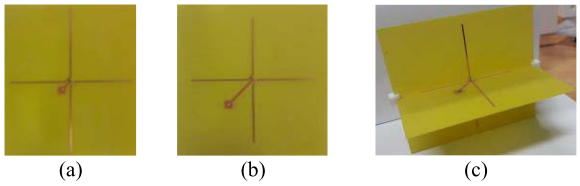


**FIGURE 8.** Photographs of the fabricated crossed dipoles and tripoles, (a): optimally-fed crossed dipole, (b): in-phase-fed crossed dipole, (c): optimally-fed tripole. The in-phase-fed tripole looks the same as the optimally-fed tripole except for $\Delta L = 0$ on the $y$-axis dipole and a longer transformer line ($L_T$).

**TABLE 4.** Dimensions of the fabricated crossed dipoles and tripoles.

| Test antennas | Offsets + via | Dipole + Feed | Particularities |
|---|---|---|---|
| Optimally-fed crossed dipole | $L_O = 6.36$ $W_O = 1$ $L_S = 3.03$ $W_S = 1.2$ $d_{via} = 0.6$ | $L = 55$ $W = 1$ $L_M = 2$ $W_M = 1.55$ | $\Delta L = 11.5$, $C_M = 0\ pF$ $L_T = 9.37$, $W_T = 0.3$ |
| In-phase-fed crossed dipole | | | $\Delta L = 0$, $C_M = 2\ pF$ $L_T = 30.61$, $W_T = 0.3$ |
| Optimally-fed tripole | | $L = 50.2$ $W = 1$ $L_M = 2$ $W_M = 1.55$ $\Delta L_z = 11$ | $\Delta L = 15.5$, $C_M = 2.6\ pF$ $L_T = 25.51$ $W_T = 0.3$ |
| In-phase-fed tripole | | | $\Delta L = 0$, $C_M = 1.5\ pF$ $L_T = 32.61$, $W_T = 0.3$ |

Dimensions are millimeters (mm).

**Step #4**. This step improves the impedance matching level by adjusting the transformer length and characteristic impedance through $L_T$ and $W_T$. A supplemental series matching capacitor ($C_M$) may be necessary to complete the impedance matching process by compensating for the inductive part of the obtained impedance.

The entire design process, involving steps #1 through #4, is carried out at the fundamental resonance of the tripole and the crossed dipole to yield the corresponding optimally-fed structures.

#### 2) THE IN-PHASE-FED CROSSED DIPOLE AND TRIPOLE

These structures have the exact dimensions as the optimally-fed crossed dipole and tripole, except for $\Delta L = 0$, setting the in-phase-fed condition. Beyond that, these structures may require a dedicated impedance matching process (step #4) due to the dipole lengths' change.

#### 3) THE FABRICATED PROTOTYPES

Table 4 gives the dimensions of the fabricated crossed dipoles and tripoles based on the previous design procedure, while Figs. 8a – 8b shows the prototypes' photographs.

### C. DUAL-BAND QUASI-ISOTROPIC ANTENNA

This antenna includes two collocated quasi-isotropic dipoles operating at two separate frequencies around 900 and 1800 MHz, as seen in Fig. 9a. The concept has been recently proposed in [33] and is scalable to more than two isotropic bands. One of the design challenges is setting up the single-port feed network. The reader is advised to refer to [33] for more details. Note that optimizing this antenna means

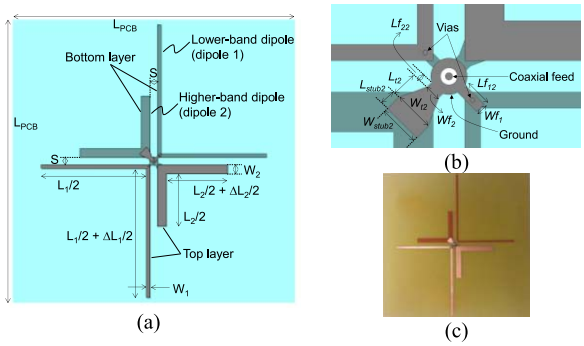


**FIGURE 9.** The dual-band quasi-isotropic antenna, (a): overview, (b): zoom in the feed network, (c): photograph of the fabricated prototype.

**TABLE 5.** Dimensions of the fabricated dual-band quasi-isotropic dipole.

| Dipole | Spacing | Feed | Extra length |
|---|---|---|---|
| $L_1 = 117$, $W_1 = 2$ | $S = 4$ | $L_{f11} = 4.65$, $L_{f12} = 3.46$, $W_{f1} = 1.3$ | $\Delta L_1 = 26$ |
| $L_2 = 58$ $W_2 = 6$ | | $L_{f21} = 3.82$, $L_{f22} = 0.76$, $W_{f2} = 2$, $L_{t2} = 3.53$, $L_{stub2} = 2$, $W_{stub2} = 5.25$ | $\Delta L_2 = 10$ |

Dimensions are millimeters (mm).

going through steps #2 to #3 in Fig. 7 for each frequency band of interest. Then, an impedance-matching process with a dedicated feed will complete the design.

As seen in Fig. 9b, the proposed feed is hybrid, with direct connections to the lower-band dipole and a coupling feed for the higher-band dipole. Please refer to [33] for more details. Table 5 shows the dimensions of the optimized prototype, while Fig. 9c presents a photograph of the fabricated prototype.

### D. MEASURED PERFORMANCES

Fig. 10 presents the fabricated test antennas' measured and simulated reflection coefficients ($S_{11}$), performed with CST [34].

The measured $S_{11}$ correlates with the simulations for all the antennas. Under $S_{11} \leq -10$ *dB*, the dipole covers the bandwidth of 894 – 996 MHz (102 MHz), while the crossed dipoles cover 804 – 990 MHz (186 MHz) and 876 – 906 MHz (30 MHz) for the optimally-fed and in-phase-fed structures, respectively. In addition, the optimally-fed tripole covers the bandwidth of 834 – 1050 MHz (216 MHz), while the in-phase-fed tripole is 830 – 967 MHz (137 MHz). Finally, the dual-band quasi-isotropic antenna addresses 815 – 1095 MHz (280 MHz) and 1650 – 2020 MHz (418 MHz).

Overall, all the test antennas cover the GSM 900 (880 – 960 MHz) at $S_{11} \leq -10$ *dB* or $S_{11} \leq -6$ *dB*, which is acceptable for mobile communications. Beyond that, the dual-band quasi-isotropic antenna covers the upper-band wireless standards, including DCS 1800 (1710-1880 MHz), PCS1900 (1850-1990 MHz), and UMTS (1920-2170 MHz).

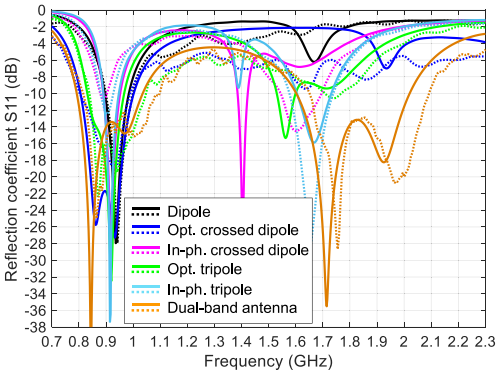


**FIGURE 10.** Measured and simulated reflection coefficients $S_{11}$ of the test antennas. The full line represents simulation, while the dotted line denotes measurement. Opt. = optimally-fed, In-ph. = in-phase-fed.

Table 6 summarizes the measured and simulated performances over the covered frequency bands. This includes efficiency, directivity, and realized gain results.

It is seen that the test antennas' measured efficiencies range between 70 and 95%, while their realized gains are within 1.08 – 3 dBi. These values correlate with simulation results at 84 – 95% and 0.8 – 1.9 dBi, respectively.

The noted differences between the measured and simulated performances are due to several factors: i) the substrate loss, which is underestimated in simulation, ii) the efficiency measurement errors inherent to the Wheeler cap approach through the cavity and antenna modes' overlappings [35], and finally iii) the measuring cable's parasitic radiation, which affects directivity and radiation patterns, not detailed for brevity. These parasitic effects increase the directivity variation ($\Delta D_{ir}$), which remains acceptable compared with simulations (Table 6).

Measurements confirm that the optimally-fed prototypes have a near-isotropic pattern in $\phi$-polarization and a null in the entire horizontal plane for $\theta$-polarization, except for the optimum tripole showing a null pair. Besides, the in-phase-fed prototypes exhibit larger null domains in both polarizations. These radiation characteristics are present over the covered frequency bands.

The following section evaluates the performances of the test antennas within a controlled propagation environment.

## IV. NUMERICAL TESTS

This section evaluates the performance of the previous test antennas within a dedicated propagation environment while controlling the incident power density under spherical incidences and polarizations. Such a controlled environment is synthesized inside a full-wave antenna simulator, typically CST [34]. One of the key features of this study is including most electromagnetic interaction phenomena between the receiving antenna and the complex incident wavefield simultaneously. Another option is testing the antennas within the exact propagation characteristics, which are not evident within the ambient environment.

**TABLE 6.** Measured and simulated performances of the test antennas.

| Test antennas | | Single dipole | Optimally-fed crossed dipole | In-phase-fed crossed dipole | Optimally-fed tripole | In-phase-fed tripole | Dual-band quasi-isotropic antenna | |
|---|---|---|---|---|---|---|---|---|
| Covered bands (Frequency) | | Single (940 MHz) | Single (940 MHz) | Single (940 MHz) | Single (940 MHz) | Single (940 MHz) | Band #1 (940 MHz) | Band #2 (1840 MHz) |
| Tot. eff. (%) | Simu. | 95.00 | 94.70 | 88.41 | 91.18 | 85.17 | 91.72 | 84.37 |
| | Meas. | 83.90 | 86.00 | 76.62 | 83.77 | 78.23 | 94.30 | 71.75 |
| Dir. (dBi) | Simu. | 2.08 | 2.07 | 2.02 | 1.62 | 1.59 | 2.13 | 2.05 |
| | Meas. | 2.38 | 1.73 | 2.39 | 3.77 | 2.73 | 1.98 | 3.16 |
| Gain (dBi) | Simu. | 1.85 | 1.83 | 1.85 | 1.22 | 0.89 | 1.75 | 1.31 |
| | Meas. | 1.62 | 1.08 | 1.65 | 3.00 | 1.67 | 1.72 | 1.72 |
| $S_{11}$-BW (MHz) | Simu. | 895-984 (89 MHz) | 804-1001 (197 MHz) | 890-952 (62 MHz) | 830-967 (137 MHz) | 890-948 (58 MHz) | 792-1036 (244 MHz) | 1602-2020 (418 MHz) |
| | Meas. | 894-996 (102 MHz) | 804-990 (186 MHz) | 876-906 (30 MHz) | 834-1050 (216 MHz) | 876-930 (54 MHz) | 815-1095 (280 MHz) | 1650-2090 (440 MHz) |
| ΔDir (dB) | Simu. | --- | 4.31 | --- | 3.61 | --- | 4.45 | 5.25 |
| | Meas. | --- | 5.99 | --- | 8.27 | --- | 8.12 | 10.13 |

Tot. eff. = total efficiency, Dir. = maximum directivity, Gain = maximum realized gain, Meas. = measurement, Simu. = simulation, $S_{11}$-BW = covered bandwidth under $S_{11} \leq -10$ dB.

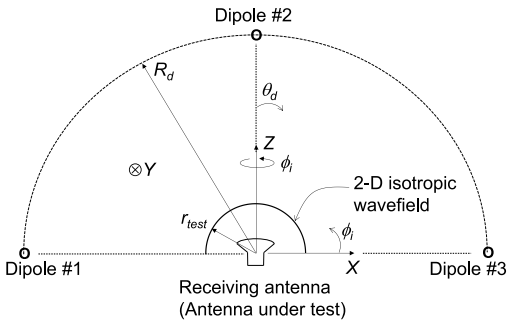


**FIGURE 11.** Simulation setup within a controlled environment inside the full-wave simulator. The array of three small dipoles synthesizes the isotropic wavefield. The dipoles are tangential to the positioning arc in the $\theta$-polarized wavefield, however, they lie orthogonally to the positioning area in the $\phi$-polarized wavefield.

### A. INCIDENT WAVEFIELD SYNTHESIS

The simulation starts by synthesizing the incident wavefield of interest in spatial distribution and power density at a specified frequency, typically 940 and 1840 MHz.

Let us consider an isotropic wavefield in both $\theta$- and $\phi$-polarizations, with a unit power density, typically $W_{inc\theta} = W_{inc\phi} = 1nW/cm^2$, providing $X = 1$. These channel characteristics are standard for most wireless applications, typically over GSM 900 and DCS 1800 bands in indoor and outdoor environments [5], [6], [9].

According to [36], synthesizing an isotropic propagation environment requires an array of three electrically small dipoles with thin or moderately thick radii, $L_d/d \geq 3$, where $L_d$ and $d$ represent the dipoles' length and diameter, respectively. Two array sets are required to cover the two polarizations while setting the dipoles' centers at the elevation angles of $\theta_d = \{-90°, 0, +90°\}$ over a radius of $R_d$, in a Cartesian coordinate system (Fig. 11).

For the $\theta$-polarized wavefield, the dipoles are tangential to the positioning arc, while in $\phi$-polarization, they lie orthogonally to the arc area. The reader is advised to refer to [36] for more details.

The dipoles are fed in phase with a feed current amplitude coefficient of $I_0$ for adjusting the power density target value. Table 7 gives the simulation setup parameters.

**TABLE 7.** Simulation setup parameters.

| Freq. (MHz) | $R_d$ | $r_{test} \approx 0.16\lambda$ | $I_0$ |
|---|---|---|---|
| 940 | 750 | 51 | 5 |
| 1840 | 750 | 26 | 0.88 |

$I_0$ is a feed current amplitude coefficient for the dipoles whose length and diameter are $L_d = 3$ mm and $d = 1$ mm, respectively.

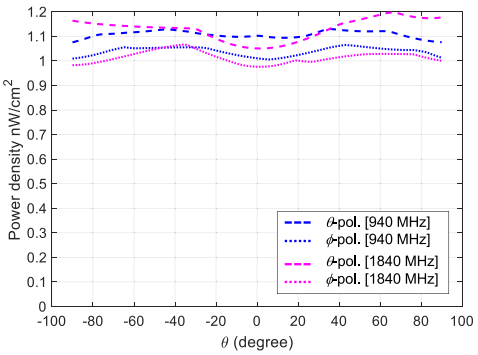


**FIGURE 12.** Synthesized isotropic wavefields at 940 and 1840 MHz in CST.

According to [36], $R_d$ should be a few wavelengths to maximize the size of the test zone ($r_{test}$) around one-tenth wavelength. Let us consider $R_d = 750$ mm, that is, 2.35λ and 4.6λ at 940 and 1840 MHz, respectively, with $r_{test} \approx 0.16\lambda$. Fig. 12 presents the calibrated wavefields at 940 and 1840 MHz.

As expected, Fig. 12 shows isotropic wavefields in both polarizations with almost a unit power density over the full incidence range of $\theta \in [-90°, 90°]$. From these results, one can compute the total available power as [36]:

$$P_{incp} = 2\pi r_{test}^2 \int_{-\pi/2}^{\pi/2} W_{inc\theta}(\theta) d\theta \tag{22}$$

where subscript $p$ indicates either $\theta$ or $\phi$-polarizations.

Table 8 compares $P_{incp}$ computed from (22) with the predicted (16), where a "1/2" factor is added to only consider the upper half hemisphere incidence.

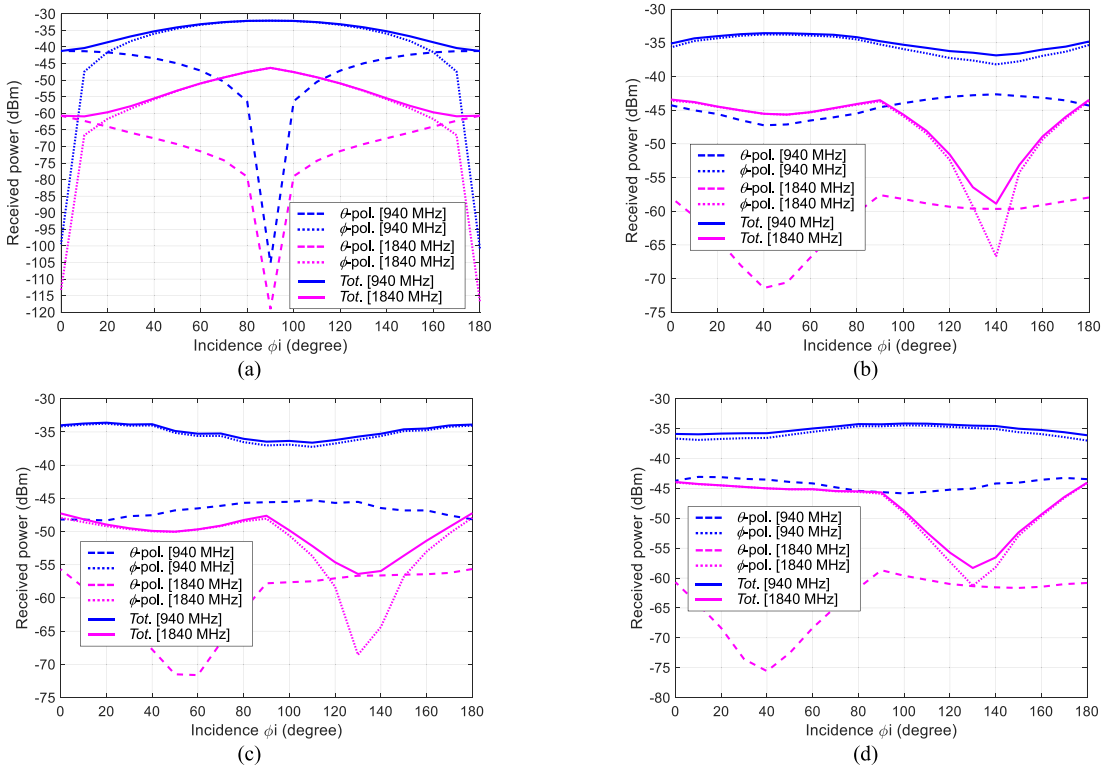


**FIGURE 13.** Received power within the synthesized isotropic wavefields at 940 and 1840 MHz in CST, (a): case of the *x*-axis dipole (b): case of the optimally-fed crossed dipole (turnstile), (c): case of the optimally-fed tripole, (d): case of the dual-band quasi-isotropic dipole. Tot. means $P_{rec\theta} + P_{rec\phi}$.

**TABLE 8.** Simulated and predicted available powers.

| Freq. (MHz) | $\theta$-polarization | | $\phi$-polarization | |
|---|---|---|---|---|
| | Simulated | Predicted | Simulated | Predicted |
| 940 | - 32.50 | - 32.92 | - 32.74 | - 32.92 |
| 1840 | -38.37 | -38.75 | -38.59 | -38.75 |

Simulated results are computed from (22). The predicted results are obtained from (16) where a "1/2" factor is added to only consider the upper half hemisphere incidence.

Table 8 shows that the predicted available power correlates with the simulated one over the two frequencies, confirming the $\lambda^2$-factor, typically 6 dB decrease from 940 to 1840 MHz.

### B. TEST ANTENNAS

The test antennas presented in Section III are now placed in the test zone, each as a receiving antenna. However, the large PCB size with FR4 ($L_{PCB} = 161.4\ mm$) sets the enclosing sphere radius at $r_{aut} \approx L_{PCB}/2 \approx 80$ mm, much larger than the test zone radius of $r_{test} \approx 51\ mm$ at 940 MHz. Therefore, the antennas are redesigned with a thicker loss-loss substrate to decrease the PCB size accordingly. The new substrate is Rogers TMM 13i, with a permittivity of $\varepsilon_r = 12.2$, a thickness of $h = 1.905\ mm$, and a loss tangent of $tan\delta = 0.0019$, stated at 10 GHz. The new PCB size is $L_{PCB} = 105\ mm$ for all antennas, setting $r_{aut} \approx 52.5\ mm$, almost equal to $r_{test} \approx 51\ mm$. Simulations show that the antennas with Rogers TMM 13i perform similarly to FR4.

### C. RESULTS

#### 1) CASE OF 2D-INCIDENT WAVEFIELDS

Each receiving antenna is sequentially rotated every $\Delta\phi_i = 10°$ in the azimuth plane to cover various incidence angles $\phi_i$ from 0 to 180° under a given illumination frequency. The received power is recorded for every incidence plane successively.

Figs. 13a – 13d illustrates some test antennas' received powers, typically the *x*-axis dipole, the turnstile, the optimum tripole, and the dual-band quasi-isotropic dipole.

Fig. 13a shows that the *x*-axis dipole receives the maximum power in $\phi$-polarization at $\phi_i = 90°$, whereas the power received in $\theta$-polarization almost vanishes. These observations cover the two frequencies. Indeed, the maximum power reception corresponds to a "perfect" alignment of the *x*-axis dipole's polarization (*x*-axis) and maximum gain with the incident wavefield's polarization and spatial distribution. In contrast, the minimum reception corresponds to a complete polarization misalignment between the channel and the *x*-axis dipole.

In addition, Fig. 13a shows a lower received power at 1840 MHz than at 940 MHz, consistent with performance decrease (gain, efficiency) with frequency.

Overall, the received powers' profiles follow the test antennas' 3D-radiation patterns, as noted in Figs. 13a – 13d.

Besides, one notes a more steady received power profile at 940 MHz for the three quasi-isotropic antennas (turnstile, optimum tripole, dual-band dipole) than the dipole. Furthermore, this stability extends at 1840 MHz for the dual-band dipole, except for a "rapid" deep around $\phi_i = 130°$, corresponding to destructive interference from the feed network's parasitic radiation. Except for the dipole, negating a feed network in simulation (lumped port), this phenomenon predominantly occurs at 1840 MHz for all the test antennas around the feed network's location.

#### 2) CASE OF 3D-INCIDENT WAVEFIELDS

The power received by the test antenna under the 3D-incident wavefield is the collection of powers received from each incidence plane, $P_{rec}(\phi_i)$. Therefore, the total power received in $p$-polarization is:

$$P_{recp} = \sum_{\phi i=0}^{180} P_{recp}(\phi_i) \tag{23}$$

Applying (23) for each test antenna in both $\theta$- and $\phi$-polarizations under the two illumination frequencies provides the results in Table 9, analyzed in the following points, first focusing on 940 MHz results:

i) Except for the $z$-axis dipole, all the antennas receive almost the same total power, $P_{rec\theta} + P_{rec\phi}$, consistent with the well-known result in [7] setting the mean effective gains of any arbitrary antennas identical within an isotropic channel.
ii) The $z$-axis dipole receives the lowest powers for two reasons: first, the incident wavefields illuminate the test antennas only from the upper half hemisphere, avoiding the lower half-dipole. Secondly, regardless of the incidence plane, the $\theta$-polarized incident wavefield is not well aligned with the dipole's polarization ($z$-axis). At the same time, the dipole poorly receives the $\phi$-polarized incident wavefield.
iii) The powers separately received by the $x$-axis, $y$-axis, and $z$-axis dipoles are almost the same as those received by the 2-port crossed dipole and the 3-port tripole. This confirms the forecasts in Sections III-A3–III-A4, claiming that the 3-port tripole and 2-port crossed dipole can be viewed as separate orthogonal dipoles.
iv) Among single-port dipole associations (crossed dipole, tripole), the optimally-fed structures receive up to 1 dB more power than the in-phase-fed structures.
v) Two optimum designs emerge, as presented in Figs. 14a – 14b. The first options are quasi-isotropic antennas: single and dual-band designs. While the second option consists in adding an $N$-way power combiner to either the 3-port tripole or the 2-port crossed dipole to combine the power received by each dipole. This collocated LP-port diversity system will outperform quasi-isotropic antennas as long as the insertion loss $IL(dB)$ in the power combiner is lower than the combining gain ($10\log n$), that is, $10\log n - IL > 0$, where $n$ is the number of antenna ports receiving significant and comparable powers ($n \leq N$). According to Table 9, it is clear that $n \approx 2$ for both the 3-port tripole and the 2-port crossed dipole.
vi) Finally, the dual-tone received power (1840 + 940 MHz) by the dual-band quasi-isotropic antenna is almost equal to its lower frequency received power (940 MHz). The $\lambda^2$-factor on the available power explains this negligible contribution from 1840 MHz under the same $W_{inc}$. This also stands for the other antennas, even though they are not necessarily well-matched and efficient on this higher frequency. Therefore, as mentioned in Section II-D, it is worth emphasizing that the multi-band design option benefits lower frequencies or those with significant power densities to compensate for the $\lambda^2$-factor.

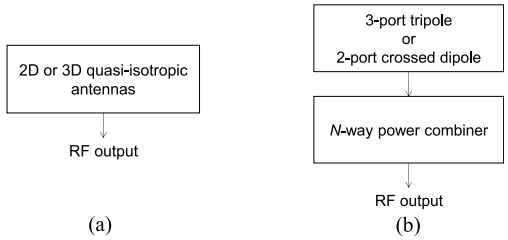


**FIGURE 14.** Optimum receiving antennas, (a): quasi-isotropic antennas, (b): collocated LP-port diversity system. LP = linearly polarized.

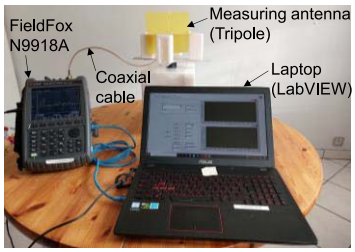


**FIGURE 15.** Photograph of the measurement setup for ambient tests.

The following section deals with real ambient tests.

## V. EXPERIMENTS IN REAL AMBIENT ENVIRONMENTS

This section deals with experiments in real ambient environments to compare the test antennas' performances, typically their time-averaged received powers.

### A. AMBIENT TESTS

#### 1) MEASUREMENT SETUP

The measurement setup includes the fabricated test antennas in Section III, a 60 cm-long 50Ω-coaxial cable, and a spectrum analyzer, model FieldFox N9918A from Keysight, as presented in Fig. 15.

A standard personal computer (PC) with a dedicated LabVIEW program controls the spectrum analyzer (SA) for automated power acquisitions.

**TABLE 9.** The test antennas' simulated received powers in both $\theta$- and $\phi$-polarizations under multi-tone 3D-isotropic wavefields.

| | Freq. (MHz) | 940 | | | 1840 | | | 940 + 1840 |
|---|---|---|---|---|---|---|---|---|
| **Test antennas** | Placement | $P_{rec\theta}$ | $P_{rec\phi}$ | $\boldsymbol{P_{recTot}}$ | $P_{rec\theta}$ | $P_{rec\phi}$ | $\boldsymbol{P_{recTot}}$ | $\boldsymbol{P_{recTot}}$ |
| Single dipole | $x$-axis | -38.70 | -30.11 | **-29.55** | -60.57 | -46.87 | **-46.68** | **-29.47** |
| | $y$-axis | -39.15 | -29.65 | **-29.19** | -61.38 | -46.07 | **-45.95** | **-29.10** |
| | $z$-axis | -72.78 | -76.82 | **-71.34** | -84.39 | -86.03 | **-82.12** | **-70.99** |
| Optimally-fed crossed dipole (turnstile) | $xy$-plane | -39.19 | -30.14 | **-29.63** | -55.02 | -40.77 | **-40.61** | **-29.30** |
| In-phase-fed crossed dipole | $xy$-plane | -39.80 | -30.72 | **-30.21** | -56.33 | -41.96 | **-41.81** | **-29.92** |
| 2-port crossed dipole | Port #1 ($x$-axis) | -38.69 | -30.09 | **-29.53** | -60.45 | -46.84 | **-46.66** | **-29.44** |
| | Port #2 ($y$-axis) | -39.18 | -29.60 | **-29.15** | -60.99 | -45.68 | **-45.56** | **-29.05** |
| Optimally-fed tripole (Optimum tripole) | $xyz$-axes | -41.43 | -29.92 | **-29.62** | -53.18 | -45.19 | **-44.55** | **-29.48** |
| In-phase-fed tripole | $xyz$-axes | -43.28 | -30.80 | **-30.56** | -59.81 | -48.24 | **-47.95** | **-30.49** |
| 3-port tripole | Port #1 ($x$-axis) | -39.91 | -29.91 | **-29.58** | -65.21 | -57.01 | **-56.40** | **-29.57** |
| | Port #2 ($y$-axis) | -40.49 | -29.55 | **-29.21** | -62.26 | -52.08 | **-51.68** | **-29.18** |
| | Port #3 ($z$-axis) | -74.05 | -80.17 | **-73.10** | -92.22 | -87.96 | **-86.58** | **-72.91** |
| Dual-band quasi-isotropic dipole | $xy$-plane | -38.95 | -30.37 | **-29.81** | -57.06 | -41.37 | **-41.25** | **-29.51** |

Simulations are performed within CST with synthesized 2D-isotropic wavefields covering the spherical incidences $\theta \in [-90°, 90°]$ in both $\theta$- and $\phi$-polarizations. The 3D-isotropic wavefields are obtained by successive 10°-azimuthal rotations of the test antennas to cover the incidences $\phi_i \in [0°, 180°]$. $P_{recTot} = P_{rec\theta} + P_{rec\phi}$.

### 2) ACQUISITION

The embedded LabVIEW software on the PC allows setting some of the key measurement parameters, defined as follows: frequency band: 0.6 – 3 GHz, Number of points: 401, sweep mode: continuous, amplitude type: power (dBm), video bandwidth (VBW): 10 kHz, resolution bandwidth (RBW): 10 kHz, Attenuation: 0 dB, and Preamplifier: Off. Under these settings, the SA's noise floor decreases to around – 90 dBm, which is decent for measuring low-power signals in the ambient environment. It is worth mentioning that any maximum power tracking function is deactivated during measurements to get ambient power's "real" time-varying behavior. The system stores the received power every 10 seconds to reach 50 measured samples with each test antenna. Each sample includes all the frequency points. All the antennas are measured on the same support the exact day between 10 – 12 am before changing the location.

### 3) LOCATIONS

Three locations with different RF propagation conditions are considered, as seen in Figs. 16a – 16c.

Location #1 is a relatively dense suburban area of separated houses in Sotteville-lès-Rouen, a town close to Rouen from the south. France's four most popular mobile service providers operate in this location. The closest RF transmitters are from SFR at 130 m from the measurement location. SFR operates over several bands, such as LTE 20: 791 – 862 MHz, GSM 900: 880 – 960 MHz, DCS 1800: 1710 – 1880 MHz, PCS 1900: 1850 – 1990, IMT 2100: 1920 – 2170 MHz, and IMT-E: 2500 – 2690 MHz [37].

Location #2 is downtown Rouen, within a dense area with relatively high domestic and professional buildings. The closest RF transmitters to this location are 210 m, corresponding to ORANGE, operating over the same frequency bands as Location #1.

Location #3 corresponds to one of ESIGELEC's buildings in a suburban area with dense forests and sparse buildings in Saint-Etienne-du-Rouvray, another city close to Rouen in the most southern part. The closest RF transmitters to this location are from ORANGE base stations at 340 m, operating over the same frequency bands as Locations #1 and #2. Only one mobile provider operates closely around this location, while four illuminate Locations #1 and #2.

### 4) POST-PROCESSING

Four post-processing steps apply to the raw received power samples. First, the measured samples are time-averaged for each frequency point. The second step cancels the SA's noise floor fluctuations by setting at – 90 dBm any signal equal to

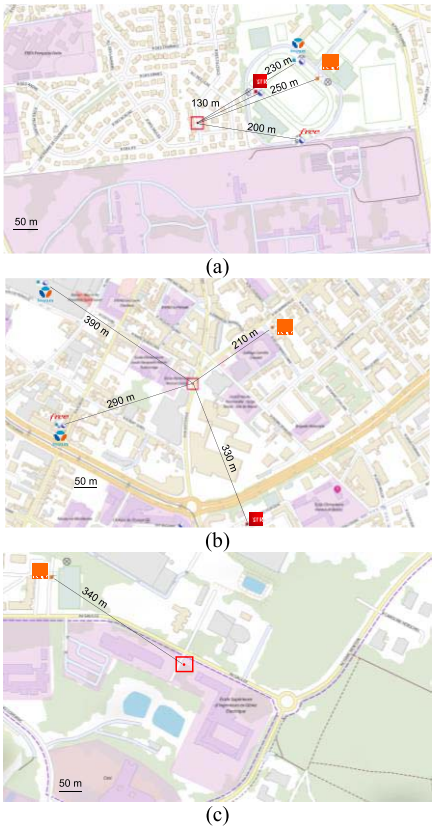


**FIGURE 16.** Maps of the locations considered for ambient tests, (a): Location #1: suburban area with dense houses, (b): Location #2: downtown Rouen with relatively high buildings, (c): Location #3: suburban area with sparse buildings and dense forests. Data from [37].

or lower than – 87 dBm, considering 3 dB noise fluctuation. The third step averages the obtained power locally on each frequency band where power exists, typically on LTE 20, GSM 900, etc. Finally, the time-averaged power on each frequency band is added to form the total time-averaged received power.

Fig. 17a shows the power received by the optimally-fed tripole over time on LTE 20 and GSM 900 bands. Furthermore, Fig. 17b presents the raw received power over the frequency domain with the post-processed steps.

One can see that the time-domain received power's profile resembles a Rayleigh fading's behavior. The cumulative distribution function (CDF), computed for the three locations over LTE 20 and GSM 900, confirms this behavior.

### 5) INCIDENT POWER DENSITY

A commercial field meter from Fields At Work, model ExpoM – RF 4 [38], is used to measure the available power densities in the three locations. First, the field meter measures the available incident field amplitude $E_{inc}$ over several center frequencies with 100 MHz bandwidth. Then, the power densities are computed as $E_{inc}{}^2/120\pi$, assuming plane wave modes.

Fig. 18 presents the measured power densities over time in Location #1, indicating a pulsed behavior for Wi-Fi signals around 2.45 GHz. However, mobile communications

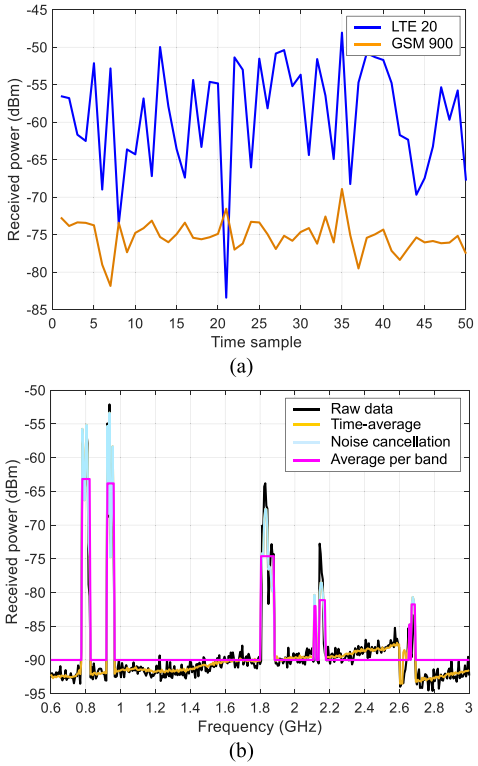


**FIGURE 17.** Power received by the optimally-fed tripole in Location #1, (a): time-domain, (b): frequency domain with post-processing steps.

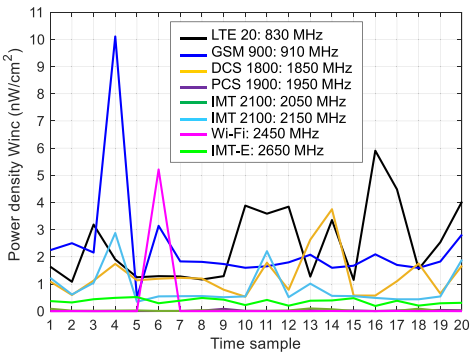


**FIGURE 18.** Measured power densities over time in Location #1 with the commercial field meter, model ExpoM – RF 4 [38]. Measurements are performed on the center frequency (MHz) with 100 MHz bandwidth.

show regular profiles, explained by downlink signals from base stations. Table 10 summarizes the time-averaged power densities in the three locations.

Table 10 shows that the time-averaged power density decreases from Locations #1 to #3, consistently with the number of RF sources and their proximity to the three locations. Besides, LTE 20 and GSM 900 show the most significant power densities in Locations #1 and #2. However, Wi-Fi power density predominates in Location #3.

Among the existing data, the work in [8] issued average power densities in London's underground at 36 and 84 nW/cm$^2$ over the downlinks of GSM 900 and DCS 1800

**TABLE 10.** Measured time-averaged power densities in the three locations.

| Location | LTE 20 | GSM 900 | DCS 1800 | IMT 2100 | Wi-Fi 2.45 GHz | IMT-E |
|---|---|---|---|---|---|---|
| #1 | 2.48 | 2.32 | 1.29 | 0.87 | 0.26 | 0.35 |
| #2 | 0.49 | 0.25 | 0.15 | 0.17 | --- | 0.11 |
| #3 | 0.05 | 0.02 | --- | 0.01 | 0.65 | --- |

Raw measurements are performed with the commercial field meter, model ExpoM – RF 4, from Fields At Work [38]. Field measurements $E_{inc}$ are time-averaged and converted to power density by $E_{inc}^2/120\pi$.

bands, respectively. These data, like those of Imperial College London (ICL) [8], are much higher than the present values. The differences may be explained by the "max-hold" function, activated during measurements, and a denser RF source distribution, as reported in [8]. Another example includes the downtown Montreal survey setting the average power over the GSM/LTE 850 band between – 30 to – 20 dBm [39], which is almost 40 dB higher than that of LTE 20 in Fig. 17b. Again, a denser RF source distribution may explain this gap. Beyond that, comparing ambient RF signal measurement data suggests including the full testing parameters to make a reliable analysis. These factors include the measurement setup (measuring antenna's gain/pattern, cable loss, etc.), the post-processing method, the location configuration (RF sources, distance from the measurement location, vegetation, etc.), weather conditions, etc.

### B. RESULTS

As described before, the total time-averaged received power is summarized in Tables 11 through 13 for the three locations for all the test antennas. In Locations #1 and #2, the total power primarily derives from the two lower bands (LTE 20, GSM 900), driving the most significant power densities. However, in Location #3, since the power density on the Wi-Fi band compensates for the $\lambda^2$-factor typically, with $(2.45/0.8)^2 \approx 9 < 0.65/0.05 \approx 13$, most of the received power derives from the Wi-Fi band, except for the turnstile (most contribution from GSM 900).

In all locations, one of the single dipole's three positions is unfavorable, minimizing the received power compared with the two other positions. This poor reception is systematic, occurring horizontally in locations #2 or vertically in Locations #1 and #3. For comparison needs, let us consider this "negative" dipole as a reference to derive the test antennas' relative power gains ($\Delta$G) within the ambient environment.

Indeed, among the single dipole's positions in the three locations, $\Delta$G rises to 4.37 dB (Location #1). The dipole's directivity and polarization misalignments explain this variation. Another point is the power imbalance between the dipole's three orthogonal positions within a given location. This is expected to limit the gain of the diversity system compared with isotropic antenna solutions. Besides, the optimally-fed tripole and crossed dipole outperform their equivalent in-phase-fed structures in all locations, confirming simulation results. Effectively, the turnstile receives up to 8 dB more power than the in-phase-fed crossed dipole. However, the optimum tripole captures up to 1.6 dB more power than the in-phase-fed tripole. These figures confirm simulation values around 1 dB.

Among quasi-isotropic antennas, the turnstile shows the best gain in Locations #1 and #3, receiving between 0.3 to 4.74 dB more power than the other antennas. This antenna's broad bandwidth, comfortably covering LTE 20 and GSM 900, explains this good performance. However, in Location #2, the dual-band quasi-isotropic dipole shows the highest power gain, 0.5 dB more than the others. Despite the dual-band option, this antenna only shows a limited gain compared with the other quasi-isotropic antennas. Therefore, the dual-band quasi-isotropic benefit is thin, targetting a higher frequency band (DCS 1800) on which the available power density does not compensate for the $\lambda^2$-factor. The three locations' results confirm this limited performance, as noted from simulations.

Finally, among all the test antennas, the turnstile reaches the best power gain of 8.37 dB (Location #3), which remains closer to the highest received powers in Locations #1 (single dipole) and #2 (dual-band dipole). The turnstile's quasi-isotropic pattern and broadband options, optimized for the lower frequency bands with significant power densities, explain this decent performance.

The following section precisely compares the two optimum antenna solutions, typically the best quasi-isotropic antenna (turnstile) and the diversity system.

### C. OPTIMUM ANTENNAS WITHIN THE AMBIENT ENVIRONMENT

Let us compare the best-optimized quasi-isotropic antenna (turnstile) with the diversity system in Fig. 14b. Table 14 summarizes the relative power gain ($\Delta$G), considering the turnstile's received power as the reference.

Table 14 shows that the diversity system, which omits insertion loss, outperforms the turnstile in Locations #1 and #2. However, the turnstile shows the highest relative power gain and beats the diversity system in Location #3. Therefore, the two antenna solutions are competitive, but the following factors mitigate the diversity system's predicted performances:

i) In practice, the power combiner introduces losses that increase with frequency and the number of ways to combine. Therefore, the designer should choose the appropriate combiner with minimum insertion loss (IL), verifying IL < $\Delta$G = 2.34 or 4.46 dB for the 2-port and 3-port dipoles, respectively. These requirements are realizable with current low-loss 2- and 3-way combiners.

**TABLE 11.** The test antennas' time-average received powers in real ambient environment in location #1.

| Test antennas | | Average received power per band – Location #1 | | | | | | Power combination | | Relative power gain ΔG (dB) |
|---|---|---|---|---|---|---|---|---|---|---|
| | Position | LTE 20 | GSM 900 | DCS 1800 | IMT-2100 | Wi-Fi 2.45GHz | IMT-E | LTE 20 + GSM 900 | All bands | |
| Single dipole | H | -65.53 | -61.29 | -80.75 | -82.13 | -83.59 | -85.12 | -59.90 | -59.80 | **4.37** |
| | H90 | -67.27 | -66.0 | -81.28 | -83.21 | -76.5 | -82.81 | -63.57 | -63.20 | **0.97** |
| | V | -67.12 | -68.47 | -76.71 | -80.65 | -79.98 | -82.05 | -64.73 | -64.17 | **0** |
| Optimally-fed crossed dipole (turnstile) | xy-plane | -63.41 | -62.90 | -75.47 | -79.78 | --- | -84.02 | -60.13 | -59.94 | **4.23** |
| In-phase-fed crossed dipole | xy-plane | -67.24 | -61.28 | -77.58 | -83.17 | --- | --- | -60.29 | -60.19 | **3.98** |
| Optimally-fed tripole | xy-plane | -63.17 | -63.82 | -74.61 | -81.13 | --- | -81.76 | -60.47 | -60.24 | **3.93** |
| In-phase-fed tripole | xy-plane | -68.31 | -63.18 | -77.41 | -82.71 | --- | -84.25 | -62.01 | -61.83 | **2.34** |
| Dual-band quasi-isotropic dipole | xy-plane | -64.54 | -64.47 | -76.89 | -81.09 | -86.63 | -83.2 | -61.49 | -61.28 | **2.89** |

H = arbitrary horizontal position, H90 = 90° rotation from H-position, V = vertical position, xy-plane = the antenna's *xy*-plane lies in the horizontal plane. Averaging applies in time domain and frequency domain per band.

**TABLE 12.** The test antennas' time-average received powers in real ambient environment in location #2.

| Test antennas | | Average received power per band – Location #2 | | | | | | Power combination | | Relative power gain ΔG (dB) |
|---|---|---|---|---|---|---|---|---|---|---|
| | Position | LTE 20 | GSM 900 | DCS 1800 | IMT-2100 | Wi-Fi 2.45GHz | IMT-E | LTE 20 + GSM 900 | All bands | |
| Single dipole | H | -75.47 | -70.24 | -84.54 | -86.68 | --- | --- | -69.1 | -68.9 | **0.62** |
| | H90 | -75.78 | -71.01 | -84.53 | -86.48 | --- | --- | -69.76 | -69.52 | **0** |
| | V | -72.9 | -70.34 | -83.33 | -86.56 | --- | -86.5 | -68.42 | -68.15 | **1.37** |
| Optimally-fed crossed dipole (turnstile) | xy-plane | -73.62 | -70.45 | -81.04 | -82.91 | --- | -86.33 | -68.74 | -68.27 | **1.25** |
| In-phase-fed crossed dipole | xy-plane | -75.83 | -70.98 | -82.18 | -86.34 | --- | --- | -69.75 | -69.41 | **0.11** |
| Optimally-fed tripole | xy-plane | -73.79 | -70.02 | -80.99 | -84.92 | --- | --- | -68.49 | -68.16 | **1.36** |
| In-phase-fed tripole | xy-plane | -74.78 | -70.97 | -80.14 | -85.21 | --- | --- | -69.45 | -68.99 | **0.53** |
| Dual-band quasi-isotropic dipole | xy-plane | -71.6 | -70.67 | -80.4 | -83.68 | --- | -86.69 | -68.09 | -67.68 | **1.84** |

ii) The diversity system's overall size, including the multi-port dipole and the power combiner, is bulky, particularly at low frequencies.
iii) In addition, the 2D or 3D dipole collocations are complex geometrical assemblies, particularly challenging to fabricate. Moreover, supplemental losses and parasitic radiations from the lines connecting the dipole ports to the power combiner should be anticipated. These limitations also apply to the simplified version of the diversity system, considering non-collocated LP dipoles at the expense of increased size.

The above issues may make the diversity solution impractical unless a DC-power combining approach is envisioned instead of RF summation [40]. Instead, like the designed turnstile, a well-optimized quasi-isotropic antenna provides competitive performances with a reduced size and a single port.

## VI. CONCLUSION

This paper dealt with the best antenna characteristics for maximally harvesting ambient waves. The proposed approach analyzed and compared key design aspects, such as multi-polarization, multi-port, multi-band, omnidirectional, quasi-isotropic, and non-quasi-isotropic pattern options, over the same antenna size.

Several test antennas covering these design aspects have been designed, fabricated, characterized, and compared within a full-wave antenna simulator under spherical incidences and polarizations. Further comparisons were based on experiments in real ambient environments.

**TABLE 13.** The test antennas' time-average received powers in real ambient environment in location #3.

| Test antennas | | Average received power per band – Location #3 | | | | | | Power combination | | Relative power gain ΔG (dB) |
|---|---|---|---|---|---|---|---|---|---|---|
| | Position | LTE 20 | GSM 900 | DCS 1800 | IMT-2100 | Wi-Fi 2.45GHz | IMT-E | LTE 20 + GSM 900 | All bands | |
| Single dipole | H | -80.18 | -78.06 | --- | --- | -76.6 | --- | -75.98 | -73.26 | **2.32** |
| | H90 | -80.01 | -78.02 | --- | --- | -76.02 | --- | -75.89 | -72.94 | **2.64** |
| | V | -84.23 | -79.85 | -86.77 | --- | -79.42 | --- | -78.49 | -75.58 | **0** |
| Optimally-fed crossed dipole (turnstile) | xy-plane | -75.61 | -68.89 | -85.8 | --- | -75.12 | --- | -68.05 | -67.21 | **8.37** |
| In-phase-fed crossed dipole | xy-plane | -83.25 | -81.52 | -84.05 | --- | -78.68 | --- | -79.28 | -75.33 | **0.25** |
| Optimally-fed tripole | xy-plane | -80.03 | -77.49 | -83.41 | --- | -74.9 | --- | -75.56 | -71.89 | **3.69** |
| In-phase-fed tripole | xy-plane | -80.62 | -77.08 | -85.22 | --- | -76.64 | --- | -75.48 | -72.76 | **2.82** |
| Dual-band quasi-isotropic dipole | xy-plane | -78.69 | -79.16 | -85.52 | --- | -74.35 | --- | -75.9 | -71.85 | **3.73** |

**TABLE 14.** Relative power gain between the best-optimized quasi-isotropic antenna (turnstile) and the collocated LP-port diversity system.

| Locations | #1 | #2 | #3 |
|---|---|---|---|
| Turnstile ($P_1$, dBm) | -60.13 | -68.74 | -68.05 |
| 2-port crossed dipole ($P_2$, dBm) | -58.34 | -66.40 | -72.92 |
| **$\Delta G = P_2 - P_1$ (dB)** | **1.79** | **2.34** | **-4.87** |
| 3-port tripole ($P_3$, dBm) | -57.44 | -64.28 | -71.86 |
| **$\Delta G = P_3 - P_1$ (dB)** | **2.69** | **4.46** | **-3.81** |

The received powers by the 2-port crossed dipole and the 3-port tripole are predicted from the single dipole's received powers in the three orthogonal positions in each location. The power combiner is assumed ideal without insertion loss.

Two optimum antenna solutions emerged from the results: the quasi-isotropic antenna and the collocated LP-port diversity system, covering lower frequency bands with significant power densities that compensate for the available power $\lambda^2$-factor.

Besides, the single-polarized dipole with an omnidirectional radiation pattern showed a systematic poor power reception among three orthogonal positions, leading to a power imbalance in the diversity system. However, the optimally-fed dipoles (crossed dipole, tripole) with quasi-isotropic patterns systematically outperformed the in-phase-fed dipoles with non-quasi-isotropic patterns.

## REFERENCES


[1] M. Wagih, A. S. Weddell, and S. Beeby, "Rectennas for radio-frequency energy harvesting and wireless power transfer: A review of antenna design [antenna applications corner]," *IEEE Antennas Propag. Mag.*, vol. 62, no. 5, pp. 95–107, Oct. 2020.

[2] C. Song et al., "Matching network elimination in broadband rectennas for high-efficiency wireless power transfer and energy harvesting," *IEEE Trans. Ind. Electron.*, vol. 64, no. 5, pp. 3950–3961, May 2017.

[3] C. Song et al., "Novel compact and broadband frequency-selectable rectennas for a wide input-power and load impedance range," *IEEE Trans. Antennas Propag.*, vol. 66, no. 7, pp. 3306–3316, Jul. 2018.

[4] M. Wagih, A. S. Weddell, and S. Beeby, "Meshed high-impedance matching network-free rectenna optimized for additive manufacturing," *IEEE Open J. Antennas Propag.*, vol. 1, pp. 615–626, 2020.

[5] W. C. Jakes, *Microwave Mobile Communications*. New York, NY, USA: Wiley, 1994.

[6] T. Taga, "Analysis for mean effective gain of mobile antennas in land mobile radio environments," *IEEE Trans. Veh. Technol.*, vol. 39, no. 2, pp. 117–131, May 1990.

[7] A. A. Glazunov, A. F. Molisch, and F. Tufvesson, "Mean effective gain of antennas in a wireless channel," *IET Microw. Antennas Propag.*, vol. 3, no. 2, pp. 214–227, 2009.

[8] M. Pinuela, P. D. Mitcheson, and S. Lucyszyn, "Ambient RF energy harvesting in urban and semi-urban environments," *IEEE Trans. Microw. Theory Techn.*, vol. 61, no. 7, pp. 2715–2726, Jul. 2013.

[9] S. Aghabeiki, "Récupération de l'énergie électromagnétique ambiante pour l'amélioration de l'autonomie des objets communicants," Ph.D. dissertation, L'Institut de Recherche en Systèmes Électroniques Embarqués, Normandie Univ., Rouen, France, 2020.

[10] A. Boaventura, D. Belo, R. Fernandes, A. Collado, A. Georgiadis, and N. B. Carvalho, "Boosting the efficiency: Unconventional waveform design for efficient wireless power transfer," *IEEE Microw. Mag.*, vol. 16, no. 3, pp. 87–96, Apr. 2015.

[11] J.-S. Park, Y.-S. Choi, and W.-S. Lee, "Design of miniaturized incident angle-insensitive 2.45 GHz RF-based energy harvesting system for IoT applications," *IEEE Trans. Antennas Propag.*, vol. 70, no. 5, pp. 3781–3788, May 2022.

[12] M. Wagih, G. S. Hilton, A. S. Weddell, and S. Beeby, "Dual-polarized wearable antenna/rectenna for full-duplex and MIMO simultaneous wireless information and power transfer (SWIPT)," *IEEE Open J. Antennas Propag.*, vol. 2, pp. 844–857, 2021.

[13] Z. Harouni, L. Cirio, L. Osman, A. Gharsallah, and O. Picon, "A dual circularly polarized 2.45-GHz rectenna for wireless power transmission," *IEEE Antennas Wireless Propag. Lett.*, vol. 10, pp. 306–309, 2011.

[14] S. Liu, D. Yang, Y. Chen, S. Huang, and Y. Xiang, "Broadband dual circularly polarized dielectric resonator antenna for ambient electromagnetic energy harvesting," *IEEE Trans. Antennas Propag.*, vol. 68, no. 6, pp. 4961–4966, Jun. 2020.

[15] V. Kuhn, C. Lahuec, F. Seguin, and C. Person, "A multi-band stacked RF energy harvester with RF-to-DC efficiency up to 84%," *IEEE Trans. Microw. Theory Techn.*, vol. 63, no. 5, pp. 1768–1778, May 2015.

[16] C. Song et al., "A novel six-band dual CP rectenna using improved impedance matching technique for ambient RF energy harvesting," *IEEE Trans. Antennas Propag.*, vol. 64, no. 7, pp. 3160–3171, Jul. 2016.

[17] S. Shen, Y. Zhang, C.-Y. Chiu, and R. Murch, "An ambient RF energy harvesting system where the number of antenna ports is dependent on frequency," *IEEE Trans. Microw. Theory Techn.*, vol. 67, no. 9, pp. 3821–3832, Sep. 2019.
[18] Z. Popović et al., "Scalable RF energy harvesting," *IEEE Trans. Microw Theory Techn.*, vol. 62, no. 4, pp. 1046–1056, Apr. 2014.
[19] J. A. Hagerty, F. Helmbrecht, W. McCalpin, R. Zane, and Z. Popović, "Recycling ambient microwave energy with broadband antenna arrays," *IEEE Trans. Microw. Theory Techn.*, vol. 52, no. 3, pp. 1014–1024, Mar. 2004.
[20] M. Wagih and S. Beeby, "Thin flexible RF energy harvesting rectenna surface with a large effective aperture for sub $\mu$W/cm2 powering of wireless sensor nodes," *IEEE Trans. Microw. Theory Techn.*, vol. 70, no. 9, pp. 4328–4338, Sep. 2022.
[21] M. Mi, M. H. Mickle, C. Capelli, and H. Swift, "RF energy harvesting with multiple antennas in the same space," *IEEE Antennas Propag. Mag.*, vol. 47, no. 5, pp. 100–106, Oct. 2005.
[22] E. Vandelle, D. H. N. Bui, T.-P. Vuong, G. Ardila, K. Wu, and S. Hemour, "Harvesting ambient RF energy efficiently with optimal angular coverage," *IEEE Trans. Antennas Propag.*, vol. 67, no. 3, pp. 1862–1873, Mar. 2019.
[23] D.-J. Lee, S.-J. Lee, I.-J. Hwang, W.-S. Lee, and J.-W. Yu, "Hybrid power combining rectenna array for wide incident angle coverage in RF energy transfer," *IEEE Trans. Microw. Theory Techn.*, vol. 65, no. 9, pp. 3409–3418, Sep. 2017.
[24] S. Shen, Y. Zhang, C.-Y. Chiu, and R. Murch, "A triple-band high-gain multibeam ambient RF energy harvesting system utilizing hybrid combining," *IEEE Trans. Ind. Electron.*, vol. 67, no. 11, pp. 9215–9226, Nov. 2020.
[25] S. R. Best and B. C. Kaanta, "A tutorial on the receiving and scattering properties of antennas," *IEEE Antennas Propag. Mag.*, vol. 51, no. 5, pp. 26–37, Oct. 2009.
[26] S. Aghabeiki, C. M. A. Niamien, and M. Kadi, "Time-average behaviors of indoor propagation channels on wireless applications," in *Proc. IEEE APS*, 2020, pp. 1165–1166.
[27] T. S. Rappaport, *Wireless Communications: Principles and Practice*. London, U.K.: Pearson, 2002.
[28] S. Hemour et al., "Towards low-power high-efficiency RF and microwave energy harvesting," *IEEE Trans. Microw. Theory Techn.*, vol. 62, no. 4, pp. 965–976, Apr. 2014.
[29] C. M. A. Niamien, "Synthesis approach of quasi-isotropic dipole arrays based on the vector effective height formulation," *IEEE Trans. Antennas Propag.*, vol. 70, no. 5, pp. 3888–3893, May 2022.
[30] "Bernier electronik." Accessed: Aug. 2022. [Online]. Available: https://bernierelectronik-boutique.fr/index.php
[31] C. A. Balanis, *Antenna Theory Analysis and Design*, 3rd ed. Hoboken, NJ, USA: Wiley, 2005.
[32] M. F. Bolster, "A new type of circular polarizer using crossed dipoles," *IRE Trans. Microw. Theory Techn.*, vol. 9, no. 5, pp. 385–388, Sep. 1961.
[33] C. M. A. Niamien, "Single-feed planar multi-band quasi-isotropic antennas through collocating and co-design approaches," *IEEE Trans. Antennas Propag.*, submitted for publication.
[34] "Dassault systemes." Accessed: Aug. 2022. [Online]. Available: https://www.3ds.com
[35] M.-C. Huynh, "Wideband compact antenna for wireless communications applications," Ph.D. dissertation, Virginia Polytech. Inst., State Univ., Blacksburg, VA, USA, 2004.
[36] C. M. A. Niamien, "2-D WFS approach through field transformation—Application to performance prediction in standard antenna simulators," *IEEE Open J. Antennas Propag.*, vol. 2, pp. 1120–1131, 2021.
[37] "Cartoradio." Accessed: Jul. 2022. [Online]. Available: https://www.cartoradio.fr/
[38] "Fields at work." Accessed: Aug. 2022. [Online]. Available: https://fieldsatwork.ch
[39] X. Gu, L. Grauwin, D. Dousset, S. Hemour, and K. Wu, "Dynamic ambient RF energy density measurements of montreal for battery-free IoT sensor network planning," *IEEE Internet Things J.*, vol. 8, no. 17, pp. 13209–13221, Sep. 2021.
[40] U. Olgun, C.-C. Chen, and J. L. Volakis, "Investigation of rectenna array configurations for enhanced RF power harvesting," *IEEE Antennas Wireless Propag. Lett.*, vol. 10, pp. 262–265, 2011.

**CONSTANT M. A. NIAMIEN** (Member, IEEE) received the M.Sc. and Ph.D. degrees in electrical engineering from the University of Rennes1, Rennes, France, in 2007 and 2010, respectively, and the "Habilitation à Diriger la Recherche" degree from the University of Rouen, France, in 2020.

He was with the Department of Antennas and Propagation, Centre of Nuclear Energy, Grenoble, France, as a Research Engineer in 2011. In addition, he was with LEMA, EPFL, Switzerland, in 2010, as an Invited Researcher. In 2012, he joined EMITECH Group, Montigny-le-Bretonneux, France, as an Engineer. He joined ESIGELEC, IRSEEM, Normandie Univ, UNIROUEN, Rouen, France, as an Associate Professor in 2012. He has been a Full Professor with ESIGELEC since December 2020. He has coauthored French patent and mainly authored more than 50 journal and conference papers edited by IEEE and IET societies and Wiley periodicals. His research fields include multi-band and broadband antennas, antenna theory, electromagnetic modeling for antenna applications, receiving antennas, metasurfaces, rectennas for wireless ambient energy harvesting applications, and material characterization.

Prof. Niamien has been the Project Coordinator of four research projects (European, Regional) for overall attracted funding of more than €4 M. He has been a scientific contributor to three research projects. He has co-chaired two IEEE conference (APS and APMC) sessions. He has been a member of the European Association on Antennas and Propagation since 2015 and a TPC Member of the "Journées Nationales Microondes" (JNM19) Caen, France.